

Recovering 3D Magnetic Turbulence from Single-Frequency Faraday Screens

A. MELNICHENKA,¹ A. LAZARIAN,² AND D. POGOSYAN³

¹*Department of Physics, Berea College, Berea, KY 40404, USA*

²*Department of Astronomy, University of Wisconsin–Madison, Madison, WI 53706, USA*

³*Department of Physics, University of Alberta, Edmonton, AB T6G 2E1, Canada*

(Received February 26, 2026)

Submitted to ApJ

ABSTRACT

Statistics of polarized synchrotron radiation carry information about the properties of the underlying turbulence. Different statistical measures constructed from observables probe turbulence properties in different ways. We consider a setup in which synchrotron radiation is emitted in a distant volume and then passes through a turbulent screen that induces Faraday rotation. Using both MHD simulations and synthetic turbulence spectra, we explore the spectrum of observed polarization directions measured at a single frequency as a diagnostic for recovering the statistics of turbulence in both the emitting region and the Faraday-rotation screen. We compare these results with our analytical expectations. We also compare the spectrum of polarization direction (SPD) with the wavelength-derivative diagnostic introduced and analytically explored by Lazarian & Pogosyan. We demonstrate that the SPD exhibits greater sensitivity to turbulence in the Faraday screen. We provide an observer-friendly criterion to determine whether the SPD samples turbulence in the synchrotron-emitting region or in the Faraday screen. These results open a practical pathway for extracting turbulence statistics from existing and forthcoming single-band radio polarimetry.

Keywords: Interstellar magnetic fields (845) — Interstellar medium (847) — Intracluster media (858) — Interstellar dynamics (839) — Magnetohydrodynamics (1964) — Turbulence (1735) — Faraday rotation (529) — Polarimetry (1278) — Numerical methods (1965)

1. INTRODUCTION

Magnetic turbulence is ubiquitous in astrophysics (Armstrong et al. 1995). Magnetic turbulence affects star formation (Federrath 2018), angular momentum transport (Balbus & Hawley 1991) and mediates conductivity and cosmic-ray propagation (Brandenburg & Lazarian 2013), yet most observational diagnostics are limited to 2D projections along the line of sight (LOS) (Elmegreen & Scalo 2004). Faraday rotation is one of the most widely used probes of these magnetized plasmas: from Galactic RM grids and pulsars to cluster radio halos and FRBs, it reveals the LOS magnetic field weighted by the thermal-electron density, and, through its spatial statistics, encodes the underlying turbulence (e.g., see the review by Akahori et al. 2018).

The development of the RM synthesis technique (Brentjens & de Bruyn 2005; Burn 1966) has greatly increased the amount of information that can be extracted from polarization observations, as it allows polarized emission to be separated by the degree of Faraday rotation it has experienced.

Recent work has tested polarization-based turbulence diagnostics in simulations and observations, including numeri-

cal validation and observational applications of synchrotron-polarization statistics (e.g., Herron et al. 2016; Zhang et al. 2016, 2023; Xiao et al. 2025). In particular, Zhang et al. (2016) explored several multi-frequency polarization measures; while in turbulence-dominated regimes the leverage they add on the inertial-range slope was found to be limited compared with direct angular two-point statistics, they showed a significant potential when a strong mean field is present.

Earlier work used synchrotron intensity and polarized intensity fluctuations to infer the spectrum and anisotropy of magnetic turbulence. Experimental observational data were available, but the theoretical understanding of these processes was provided by Lazarian & Pogosyan (2012, hereafter LP12), who derived synchrotron statistics for an arbitrary electron index and, crucially, adopted a physically motivated model of anisotropic MHD turbulence consistent with Goldreich & Sridhar (1995).

Building on this, Lazarian & Pogosyan (2016, hereafter LP16) incorporated Faraday rotation and established how synchrotron polarization statistics depend on the underlying

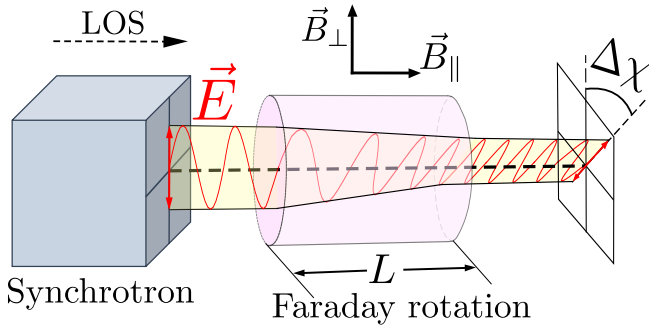


Figure 1. Schematic of the separated-screen geometry adopted in this work. Polarized synchrotron emission (gray cube), produced in a background region (e.g., a galactic halo with low thermal electron density), passes through a foreground Faraday-rotating screen (pink cylinder), where most of the rotation measure (RM) accumulates. Synchrotron emission and Faraday rotation are spatially separated. As shown, the polarization rotation due to the Faraday effect is represented by a change in the polarization angle, $\Delta\chi$, which depends on wavelength.

magnetic and electron-density fluctuations along the line of sight. LP16 developed position–position–frequency (PPF) statistics of polarized synchrotron emission and introduced Faraday-sensitive measures that involve spectral derivatives (e.g., correlations of $dP/d\lambda^2$). Such diagnostics are powerful but require accurate multi-frequency sampling to form derivatives and are not angle-native.

Here we investigate a new use of the structure function for the polarization angle χ introduced in Lazarian et al. (2022).

$$D_\chi = \frac{1}{2} \left\langle 1 - \cos 2[\chi(\mathbf{X}, \lambda^2) - \chi(\mathbf{X} + \mathbf{R}, \lambda^2)] \right\rangle, \quad (1)$$

where 2D vector \mathbf{R} refers to the separation on the sky between the two lines-of-sight (LOS).¹ Angle dispersion and angle structure function statistics have a long history in polarimetry as turbulence diagnostics and as the basis of Davis–Chandrasekhar–Fermi-type (Davis 1951; Chandrasekhar & Fermi 1953) plane-of-sky field estimates, including modern “dispersion function” refinements that treat beam and line-of-sight averaging (e.g., Falceta-Gonçalves et al. 2008; Hildebrand et al. 2009; Houde et al. 2011). In this paper, we use this statistic to study the possibility of recovering the scaling properties of MHD turbulence from a synchrotron signal that is subjected to foreground Faraday rotation. Our setup is schematically illustrated in Fig. 1.

We derive a Fourier-spectrum estimator, complementary to the angle structure function, from $\cos 2\chi$ and $\sin 2\chi$ maps obtained from normalized Stokes parameters. We call the complex representation of the maps, $u(\mathbf{X}) = \cos 2\chi(\mathbf{X}) +$

¹ Note that the measure differs from the measure introduced for the polarization angle in (Houde et al. 2009) by the multiplier 2 in the cosine argument, and the factor 1/2 in front.

$i \sin 2\chi(\mathbf{X})$, the “director” field. We then investigate the parameter space where this estimator is most robust and where limited additional frequency coverage is required.

In the Faraday screen setting, we show numerically that our director-field statistic $D_u(R; \lambda)$ recovers the inertial-range properties of the underlying 3D magnetic turbulence even at a single frequency (cf. Lazarian & Pogosyan 2016; Lazarian et al. 2017, 2022), without requiring a wavelength array or full interferometric coverage.

In this paper, we do not address the more complex case of internal Faraday depolarization in the emitting region and coupled synchrotron-emissivity and Faraday fluctuations, which is harder to interpret and invert (Burn 1966; Sokoloff et al. 1999; Lazarian & Pogosyan 2016). Our focus on the separated-screen geometry is still applicable to many astrophysical settings, e.g., extragalactic background sources seen through the Milky Way (Haverkorn 2015; Beck 2015; Taylor et al. 2009; Oppermann et al. 2012; Jansson & Farrar 2012). Figure 1 illustrates the separated-screen geometry considered in this work in which polarized synchrotron emission is produced in a background region and undergoes Faraday rotation in a distinct foreground screen.

In §2, we introduce the polarization-angle director field and define the corresponding angle-based correlation and structure-function, emphasizing their sensitivity to Faraday rotation. We also show how the same statistic can be computed efficiently in Fourier space as a directional power spectrum, and summarize the expected inertial-range scaling and two-regime behavior. In §3, we describe the numerical setup based on both ATHENAK MHD simulations and synthetic Faraday screens. We present results from the ATHENAK runs in §4 and from the synthetic screens in §5. Finally, in §6, we compare our measure with other polarization diagnostics, including LP16 polarization and derivative-based polarization measures, and discuss the regimes where each method most robustly recovers the inertial-range slope.

2. STATISTICS OF POLARIZATION

2.1. Observables and the director field

We work with Stokes maps $Q(\mathbf{X}, \lambda^2)$ and $U(\mathbf{X}, \lambda^2)$ at one observing wavelength λ . The polarization angle is

$$\chi(\mathbf{X}, \lambda^2) = \frac{1}{2} \arg(Q + iU), \quad (2)$$

defined modulo π . To respect the π -periodicity we introduce the unit director field

$$u(\mathbf{X}, \lambda^2) = e^{2i\chi(\mathbf{X}, \lambda^2)} = \frac{Q + iU}{\sqrt{Q^2 + U^2}}. \quad (3)$$

Only circular differences enter through $u(\mathbf{X}) u^*(\mathbf{X} + \mathbf{R}) = e^{2i\Delta\chi}$, so no angle unwrapping is required.

We consider a polarized background with intrinsic complex polarization $P_i = |P_i| e^{2i\psi}$ passing through a foreground

magnetized slab of thickness L . The Faraday rotation measure (RM) in CGS system units is given by

$$\Phi(\mathbf{X}) = \frac{e^3}{2\pi m_e^2 c^4} \int_0^L n_e(\mathbf{X}, z) B_{\parallel}(\mathbf{X}, z) dz, \quad (4)$$

and the angle of the observed polarization is (Burn 1966).

$$\chi(\mathbf{X}, \lambda^2) = \psi(\mathbf{X}) + \lambda^2 \Phi(\mathbf{X}). \quad (5)$$

where $\psi(\mathbf{X})$ is the phase of the source signal.

Table 1 collects the symbols used throughout the paper.

2.2. Directional correlation and angle structure function

Our basic two-point statistic is the directional correlation,

$$\xi_u(\mathbf{R}; \lambda) = \langle u(\mathbf{X}, \lambda^2) u^*(\mathbf{X} + \mathbf{R}, \lambda^2) \rangle = \langle \cos 2\Delta\chi \rangle, \quad (6)$$

and its structure function form

$$D_u(\mathbf{R}; \lambda) = 2[1 - \xi_u(\mathbf{R}; \lambda)]. \quad (7)$$

From Eq. (5), $u(\mathbf{X}, \lambda^2) = e^{2i\psi(\mathbf{X})} e^{2i\lambda^2\Phi(\mathbf{X})}$. Assuming the intrinsic polarization direction and the Faraday screen are statistically independent, the director correlation factorizes:

$$\xi_u(\mathbf{R}; \lambda) = \exp[-2D_\psi(\mathbf{R})] \exp[-2\lambda^4 D_\Phi(\mathbf{R})], \quad (8)$$

where

$$D_\psi(\mathbf{R}) = \langle [\psi(\mathbf{X} + \mathbf{R}) - \psi(\mathbf{X})]^2 \rangle \quad (9)$$

is the structure function of the intrinsic polarization phases at the source and

$$D_\Phi(\mathbf{R}) = \langle [\Phi(\mathbf{X} + \mathbf{R}) - \Phi(\mathbf{X})]^2 \rangle \quad (10)$$

is the RM structure function. Here we have assumed the Gaussian statistics for χ and Φ .

In the special case of a uniform polarized background, this reduces to

$$D_u(\mathbf{R}; \lambda) = 2 \left[1 - e^{-2\lambda^4 D_\Phi(\mathbf{R})} \right]. \quad (11)$$

In the weak-rotation limit $2\lambda^4 D_\Phi \ll 1$, this linearizes to $D_u(\mathbf{R}; \lambda) = 4\lambda^4 D_\Phi(\mathbf{R})$, so the angle structure function directly traces the RM structure function, scaled by λ^4 .

2.3. Intrinsic polarization model

The 2D projected correlation of δP_i has correlation length r_i and inertial-range index m_i .

Following LP16, we adopt a regularized isotropic model for the intrinsic polarization-angle correlations. Lazarian et al. (2022) showed that if the mean polarization dominates the fluctuations, as in a sub-Alfvénic regime, then the statistics of the polarization angle follow the scaling of the polarization itself. Thus, if we adopt the model

$$D_\psi(R) = 2\sigma_\psi^2 \frac{(R/r_i)^{m_i}}{1 + (R/r_i)^{m_i}}. \quad (12)$$

the spectral index m_i will be similar to that of the magnetic field, but projected onto the 2D plane. If the 2D source polarization is accumulated through a turbulent region of significant depth, the Kolmogorov scaling corresponds to $m_i = 1 + 2/3 = 5/3$, where the extra unity comes from integrating the 3D field along the line of sight. The intrinsic phase variance σ_ψ^2 reflects the Alfvénic Mach number of such a turbulent source, but does not exceed $1/2$.

2.4. RM model

Let $\phi(\mathbf{X}, z) \propto n_e(\mathbf{X}, z) B_{\parallel}(\mathbf{X}, z)$ be the 3D RM-density field, with rms σ_ϕ , correlation length r_ϕ , and correlation index m_ϕ , such that $\Phi(\mathbf{X}) = \int_0^L \phi(\mathbf{X}, z) dz$. The correlation index m_ϕ is related to the 3D spectral index as $P_\phi(k) \propto k^{n_\phi} \propto k^{-3-m_\phi}$, so positive $m_\phi > 0$ corresponds to steep spectra, while negative $m_\phi < 0$ corresponds to shallow RM-density spectra. The RM density spectrum is expected to be steep when it is dominated by the fluctuations of the B_{\parallel} on a background of relatively uniform density of thermal electrons (Kolmogorov scaling is $m_\phi = 2/3$), but can become shallow when density fluctuations are important.

For a thick Faraday screen ($L \gg r_\phi$), LP16 show that for $R \ll r_\phi$,

$$D_\Phi(R) = 2\sigma_\phi^2 L r_\phi^{-m_\phi} R^{1+m_\phi}, \quad (13)$$

so the RM structure function scales as $D_\Phi(R) \propto R^{1+m_\phi}$ in this regime. We will use the regularized ansatz

$$D_\Phi(R) = 2\sigma_\Phi^2 \frac{(R/r_\phi)^{m_\Phi}}{1 + (R/r_\phi)^{m_\Phi}}, \quad (14)$$

where $\sigma_\Phi^2 = \sigma_\phi^2 L r_\phi$ is the saturated RM variance. This ansatz can be used for $0 < m_\Phi < 2$ which corresponds to the RM density spectrum in $-4 < n_\phi < -2$ range.

2.5. Weak-rotation expansion and the two-slope regime

We now expand the factorized director correlation (Eq. 8) in the regime where both intrinsic decorrelation and Faraday rotation are small. For weak decorrelation (small D_ψ and small $2\lambda^4 D_\Phi$), we expand each factor to leading order:

$$e^{-2\lambda^4 D_\Phi} = 1 - 2\lambda^4 D_\Phi \quad (15)$$

Therefore

$$\xi_u = 1 + \sigma_\psi^2 - \frac{1}{2} D_\psi - 2\lambda^4 D_\Phi \quad (16)$$

and hence

$$D_u = D_\psi + 4\lambda^4 D_\Phi \quad (17)$$

substituting (12) and (14) we obtain the expanded form of directional structure function

$$\frac{D_u}{2} = \sigma_\psi^2 \frac{(R/r_i)^{m_i}}{1 + (R/r_i)^{m_i}} + \eta^2 \frac{(R/r_\phi)^{m_\Phi}}{1 + (R/r_\phi)^{m_\Phi}} \quad (18)$$

Table 1. Parameters for the correlation studies of synchrotron polarization in separated emitting and Faraday-rotating regions.

Parameter	Meaning	First appearance
\mathbf{X}, \mathbf{R}	2D sky position; 2D separation ($R = \mathbf{R} $)	Eqs. (3), (6)
$\chi(\mathbf{X}, \lambda^2); u = e^{2i\chi}$	Polarization angle (mod π); unit director field	Eq. (3)
$P_i(\mathbf{X}); \Phi(\mathbf{X}); \phi(\mathbf{X}, z)$	Intrinsic complex polarization; Faraday rotation measure (RM); RM density	Eqs. (5), (4); §2.4
$\xi_u(R; \lambda); D_u(R; \lambda)$	Director correlation and structure function	Eqs. (6), (7)
$D_\psi(R); D_\Phi(R)$	Intrinsic-phase; RM structure functions	Eq. (8)
Scales:		
$\lambda; L$	Observing wavelength; LOS depth of Faraday screen	Eqs. (3), (4)
$r_i; r_\phi$	Correlation lengths of intrinsic polarization and RM density	Eqs. (12), (13)
$R_\times; k_\times$	Domain-boundary separation and wavenumber	Eqs. (22), (23)
Spectral indices:		
$m_i; m_\phi; m_\Phi$	Intrinsic; RM-density; RM exponents	Eqs. (12), (13), (14)
Basic statistics:		
$\eta = 2\sigma_\Phi \lambda^2$	Faraday rotation strength	Eqs. (18), (19)
$\sigma_\phi; \sigma_\Phi$	rms RM-density; rms RM (saturated)	Eqs. (13), (14)

where the dimensionless coefficient

$$\eta = 2\sigma_\Phi \lambda^2 \quad (19)$$

describes the Faraday rotation strength in terms of the average rotation angle (in radians) through the Faraday region.

In Eq. (18) the first term is the intrinsic (synchrotron-angle) contribution and the second is the Faraday contribution. If $m_i \neq m_\Phi$ one can observe the characteristic scale R_\times where the director structure function changes the slope. If the transition happens in the inertial range, $R \ll r_i$ and $R \ll r_\phi$, where

$$\frac{D_u}{2} \approx \sigma_\psi^2 \left(\frac{R}{r_i}\right)^{m_i} + \eta^2 \left(\frac{R}{r_\phi}\right)^{m_\Phi} \quad (20)$$

Domain boundary.—Define $R_\times(\lambda)$ by the equality of the two inertial-range terms in Eq. (20):

$$\frac{D_\psi(R_\times)}{\sigma_\psi^2} = 4\lambda^4 D_\Phi(R_\times). \quad (21)$$

The common factor σ_ψ^2 cancels. Solving for R_\times (assuming $m_\Phi \neq m_i$),

$$R_\times(\lambda) = \left(\frac{r_\phi^{m_\Phi}}{\eta^2 r_i^{m_i}}\right)^{1/(m_\Phi - m_i)}. \quad (22)$$

Hence $R_\times \propto \lambda^{-4/(m_\Phi - m_i)}$: increasing the observing wavelength shrinks the intrinsic-dominated domain and expands the Faraday-dominated one.

The corresponding domain-boundary wavenumber follows from $k_\times \sim 1/R_\times$:

$$k_\times(\lambda) \propto \lambda^{4/(m_\Phi - m_i)}. \quad (23)$$

Figure 2 shows the structure function $D_u(R; \lambda)/2$ for this configuration at several values of η . There are two domains:

at separations $R < R_\times$, the shallower of the two power laws dominates; at $R > R_\times$, the steeper one takes over. The crossover scale R_\times shifts with η exactly as predicted by Eq. (22).

2.6. Directional spectrum

Define the director components

$$n_1 = \cos 2\chi, \quad n_2 = \sin 2\chi. \quad (24)$$

Then $\xi_u(R; \lambda) = \langle n_1 n_1' \rangle + \langle n_2 n_2' \rangle$, where primes denote evaluation at $\mathbf{X} + \mathbf{R}$. By the Wiener–Khinchin theorem, ξ_u is the inverse FFT of the directional power spectrum

$$P_u(\mathbf{k}, \lambda) = |\widehat{n}_1(\mathbf{k})|^2 + |\widehat{n}_2(\mathbf{k})|^2 = \left| \mathcal{F} \left[\frac{Q + iU}{\sqrt{Q^2 + U^2}} \right] \right|^2. \quad (25)$$

Its ring average is $P_u(k, \lambda)$. This implementation requires only a single FFT of the complex director map, avoids angle unwrapping, and avoids pairwise averaging.

2.7. Hankel transform and slope identification

To translate the real-space two-slope structure (Eq. 20) into Fourier space, we use the standard 2D Hankel scaling: $\int R^m J_0(kR) R dR \propto k^{-(m+2)}$. The two inertial-range terms in Eq. (20) therefore contribute

$$P_u(k; \lambda) \propto \sigma_\psi^2 r_i^{-m_i} k^{-(m_i+2)} + \eta^2 r_\phi^{-m_\Phi} k^{-(m_\Phi+2)} + \dots \quad (26)$$

in the inertial k -range. Therefore, if $m_\Phi < m_i$, the Faraday term ($\propto k^{-(m_\Phi+2)}$) is shallower and dominates at $k \gg k_\times$ (small scales), while the intrinsic term dominates at $k \ll k_\times$. If $m_\Phi > m_i$, the Faraday term dominates at $k \ll k_\times$ (large scales).

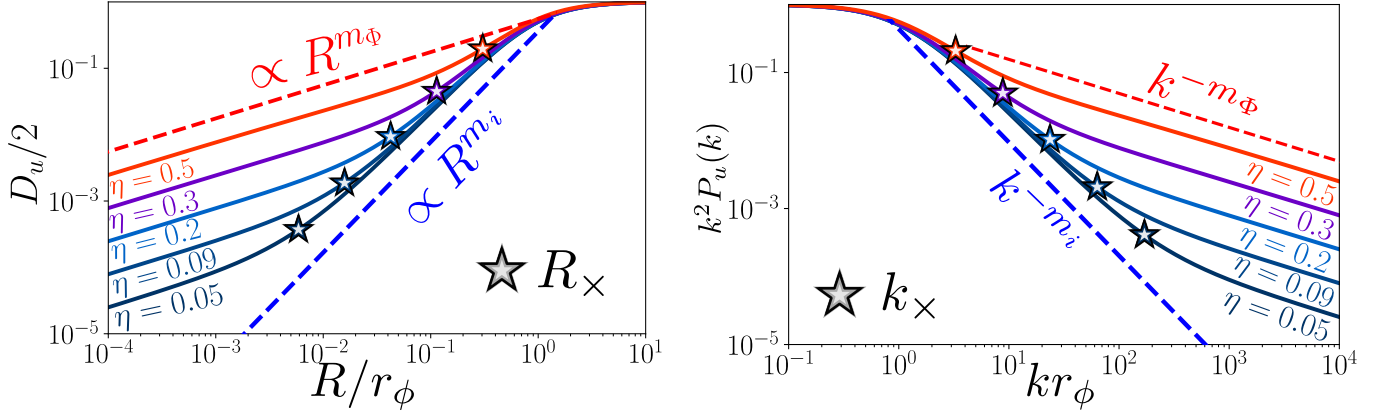


Figure 2. *Left:* The analytical expectation of the structure function $D_u(R; \lambda)/2$, predicted by Eq. (18), as a function of separation R for the density-only synthetic Faraday screen at several values of η (colored curves from $\eta = 0.05$ in blue to $\eta = 0.5$ in red). Dashed lines indicate the intrinsic ($\propto R^{m_i}$, blue) and Faraday ($\propto R^{m_\Phi}$, red) inertial-range asymptotics of the ansatz (20). The \star marks the crossover scales R_\times and k_\times , predicted by Eqs. (22) and (23). As η varies, R_\times shifts accordingly and lies at the transition between the Faraday-dominated ($\propto m_\Phi$) and intrinsic ($\propto m_i$) regimes. *Right:* The smoothed power-spectrum proxy $\mathcal{M}(k) \propto k^2 P_u(k)$ (Eq. (27)) for the same parameter set. Dashed lines show the corresponding k^{-m_i} and k^{-m_Φ} scalings. The \star on the right panel denotes the crossover scale k_\times .

2.8. Smoothed power-spectrum proxy $\mathcal{M}(k)$

To identify inertial-range slopes in Fourier space for the synthetic-screen figures we use a spectrum proxy $\mathcal{M}(k)$ constructed directly from the real-space structure function that is plotted in Fig. 2.

$$\mathcal{M}(k) = \int \frac{D_u(R; \lambda)}{2} W_{\sigma_{\ln}}(\ln(kR)) d \ln R, \quad (27)$$

with a normalized Gaussian window in $\ln(kR)$,

$$W_{\sigma_{\ln}}(x) = \frac{1}{\sqrt{2\pi} \sigma_{\ln}} \exp\left(-\frac{x^2}{2\sigma_{\ln}^2}\right), \quad x = \ln(kR), \quad (28)$$

where σ_{\ln} is the smoothing width. Because $W_{\sigma_{\ln}}$ is localized around $kR = 1$, a real-space power law $\frac{D_u}{2} \propto R^m$ maps to

$$\mathcal{M}(k) \propto k^{-m} \quad (29)$$

(up to a constant factor set by σ_{\ln}), so the two inertial-range branches in Eq. (20) appear as the reference scalings k^{-m_i} and k^{-m_Φ} in Fig. 2. The shallower branch dominates at $k \gg k_\times$ and the steeper branch dominates at $k \ll k_\times$, with $k_\times \sim 1/R_\times$. $\mathcal{M}(k)$ is defined over a logarithmic measure. Its scaling index is related to the scaling index of P_u from Eq. (25) by the addition of 2, $k^{-2-m} \rightarrow k^{-m}$.

3. NUMERICAL SETUP

We test our analytical predictions with two complementary numerical approaches. First, we run self-consistent MHD simulations with ATHENA-K to obtain physically realistic turbulent fields (§3.1). Second, because the MHD simulations have a limited inertial range (~ 1 decade on a 512^3 grid), we construct synthetic Faraday screens with prescribed spectral slopes on larger grids, giving us a wider dynamic range and full control over the intrinsic and Faraday exponents (§3.2).

Run	M_s	M_A	β	Resolution
A0	1.0	0.8	1.28	512^3
A1	10.0	0.8	0.0128	512^3

Table 2. Setups of MHD turbulence simulations. The sonic and Alfvén Mach numbers, i.e., M_s and M_A , are the instantaneous RMS values at each snapshot that is taken. $\beta = 2(M_A/M_s)^2$ is plasma magnetization.

3.1. AthenaK MHD simulations

The MHD data sets were generated with ATHENA-K (Stone et al. 2024), which solves the standard compressible ideal MHD equations under periodic boundary conditions and an isothermal equation of state with sound speed $c_s = 1$. Turbulence is driven solenoidally at a peak wavenumber $k_{\text{drive}} = 2 \times 2\pi/L_{\text{box}}$. The computational domain is a 512^3 periodic cube with $L_{\text{box}} = 1$. Details of the numerical setup and turbulence driving follow Hu et al. (2024).

The sub-Alfvénic condition ($M_A < 1$) ensures a strong mean magnetic field, so that the intrinsic polarization phase is well-described by the linearized regime $|\delta P_i| \ll |\bar{P}_i|$ discussed in §2.3.

From each snapshot we construct the intrinsic complex polarization by integrating the transverse magnetic field along the LOS (z -axis):

$$P_i(\mathbf{X}) \propto \sum_z (B_x + iB_y)^2 \Delta z, \quad (30)$$

and the Faraday rotation measure from the front portion of the box (the “screen”, occupying the first quarter of the LOS depth):

$$\Phi(\mathbf{X}) = \kappa \sum_{z=0}^{z_{\text{scr}}} n_e(\mathbf{X}, z) B_z(\mathbf{X}, z) \Delta z, \quad (31)$$

where κ is a normalization constant. The emission region extends over the remaining three-quarters of the box. The observed polarization is $P(\mathbf{X}, \lambda^2) = P_i e^{i\eta\Phi}$, where $\Phi = \Phi/\sigma_\Phi$ is the RM map normalized to unit variance and $\eta = 2\lambda^2\sigma_\Phi$ is the dimensionless rotation parameter (labeled “ η ” in the figures). We then form the director field $u = P/|P|$ and compute both $D_u(R; \lambda)$ and $P_u(k; \lambda)$ via Eq. (25).

3.2. Synthetic Faraday screens

The ATHENAK simulations have a limited inertial range (~ 1 decade), which makes precise slope fitting and identification of the two-slope regime difficult. To overcome this, we generate synthetic turbulent cubes on 1024^3 grids with prescribed spectral slopes, allowing us to control m_i and m_Φ independently and verify the analytical predictions over a wider dynamic range.

The density field is generated as a Gaussian random field in Fourier space with a prescribed 3D power spectrum $P_n(k) \propto k^{-2.26}$ (consistent with the compressible density spectrum measured in the ATHENAK runs), then exponentiated to produce a lognormal field with $\langle n_e \rangle = 1$ and $\sigma_n/\langle n_e \rangle \approx 2$, matching the statistics of the $M_s \approx 10$ simulation. The perpendicular magnetic field components (B_x, B_y) are generated as independent Gaussian random fields with Kolmogorov power spectrum $P_B(k) \propto k^{-11/3}$, and a strong mean field \bar{B}_x is added to set $M_A < 1$. From these cubes we construct $P_i(\mathbf{X})$ using the same kernel as Eq. (30), and the Faraday rotation measure $\Phi(\mathbf{X}) = \kappa \sum_z n_e B_z \Delta z$.

To isolate the Faraday response and systematically test the two-slope prediction, we consider two configurations:

1. Density-only screen: We fix $B_{\parallel} = \text{const}$ in the Faraday screen, so that $\Phi \propto \int n_e dz$. This cleanly separates the Faraday exponent m_Φ (set by the density spectrum) from the intrinsic exponent m_i (set by the perpendicular magnetic field), and reveals the two-slope regime without ambiguity.
2. Full screen: We include fluctuations of B_{\parallel} in the screen, which is more realistic and allows direct comparison with the ATHENAK results, but mixes the density and B_{\parallel} spectra in the RM density.

4. RESULTS OF ATHENAK MHD SIMULATIONS

Figure 3 shows the directional spectrum $P_u(k; \lambda)$ from the ATHENAK run with $M_A = 0.8$ with $M_s = 1.0$ and $M_s = 10$ with significant Faraday rotation $\eta = 1$. The results are shown alongside the energy spectra of the density, magnetic field, and RM.² At weak rotation the spectrum traces the intrinsic slope: for Kolmogorov turbulence the 2D directional power scales as $kP_u(k) \propto k^{-8/3}$ (Lazarian & Pogosyan

2016). As η increases, the result depends on the imprint of density fluctuations on the RM measure. If it is weak, as in $M_s = 1$ simulation, and RM measure is dominated by the magnetic field, its scaling is similar to Kolmogorov and Faraday rotation does not have a pronounced signature. For high sonic Mach number, $M_s = 10$, density, and the result RM, spectrum is shallow, $\propto k^{-2}$, and Faraday-dominated regime appears at high k reflecting this scaling, with the transitional scale k_\times shifting to lower k as predicted by Eq. (23). The limited inertial range of the 512^3 grid (~ 1 decade) prevents precise two-slope fitting, motivating the synthetic tests below.

5. RESULTS OF SYNTHETIC SIMULATIONS

We first examine the density-only screen described in §3.2. Because we prescribe $\beta_B = 11/3$ and $\beta_n = 2.26$ independently, the resulting exponents m_i and m_Φ are distinct and known a priori.

Figure 4 shows the corresponding directional spectrum $P_u(k; \lambda)$ computed from the analytic structure function model via Hankel transforms. The two inertial-range slopes ($m_i + 2$ and $m_\Phi + 2$) and the domain boundary k_\times are clearly resolved over more than two decades in k — a significant improvement over the MHD simulations.

To make a closer comparison with the self-consistent ATHENAK results, we now include fluctuations of the parallel magnetic field in the Faraday screen ($\Phi \propto \int n_e B_{\parallel} dz$). The effective RM-density spectrum is then a convolution of the density and B_{\parallel} spectra, which broadens the transition between the two slopes but does not destroy the two-regime structure. The slopes m_i and m_Φ remain recoverable, and R_\times continues to follow the scaling of Eq. (22).

6. COMPARISON WITH ALTERNATIVE MEASURES IN THE SEPARATED-SCREEN REGIME

To place our angle-based directional spectrum in context, we compare it with the two principal diagnostics from LP16: the polarization structure function $D_P(R)$ and the $dP/d\lambda^2$ correlation. The comparison is shown in Fig. 6.

6.1. Polarization structure function

In the separated-screen geometry, the polarization correlation factorizes (cf. Eq. 8) as

$$\langle P(\mathbf{X}) P^*(\mathbf{X} + \mathbf{R}) \rangle = \xi_{P_i}(\mathbf{R}) \exp[-2\lambda^4 D_\Phi(R)], \quad (32)$$

where ξ_{P_i} is the full (amplitude-weighted) intrinsic polarization correlation. As the result the correlation statistics is heavily weighted towards the regions with high polarization, losing the directional information from low polarization LOS. By contrast, our directional spectrum P_u is based on the amplitude-normalized field $u = P/|P|$ and responds more directly to Faraday rotation by focusing on the direction of the polarization. This makes P_u a more aggressive Faraday-screen probe at wider range wavelengths.

² Energy spectrum differs from the power spectrum by k^2 factor in 3D and k factor in 2D, thus we show $kP_u(k)$ to compare the scalings

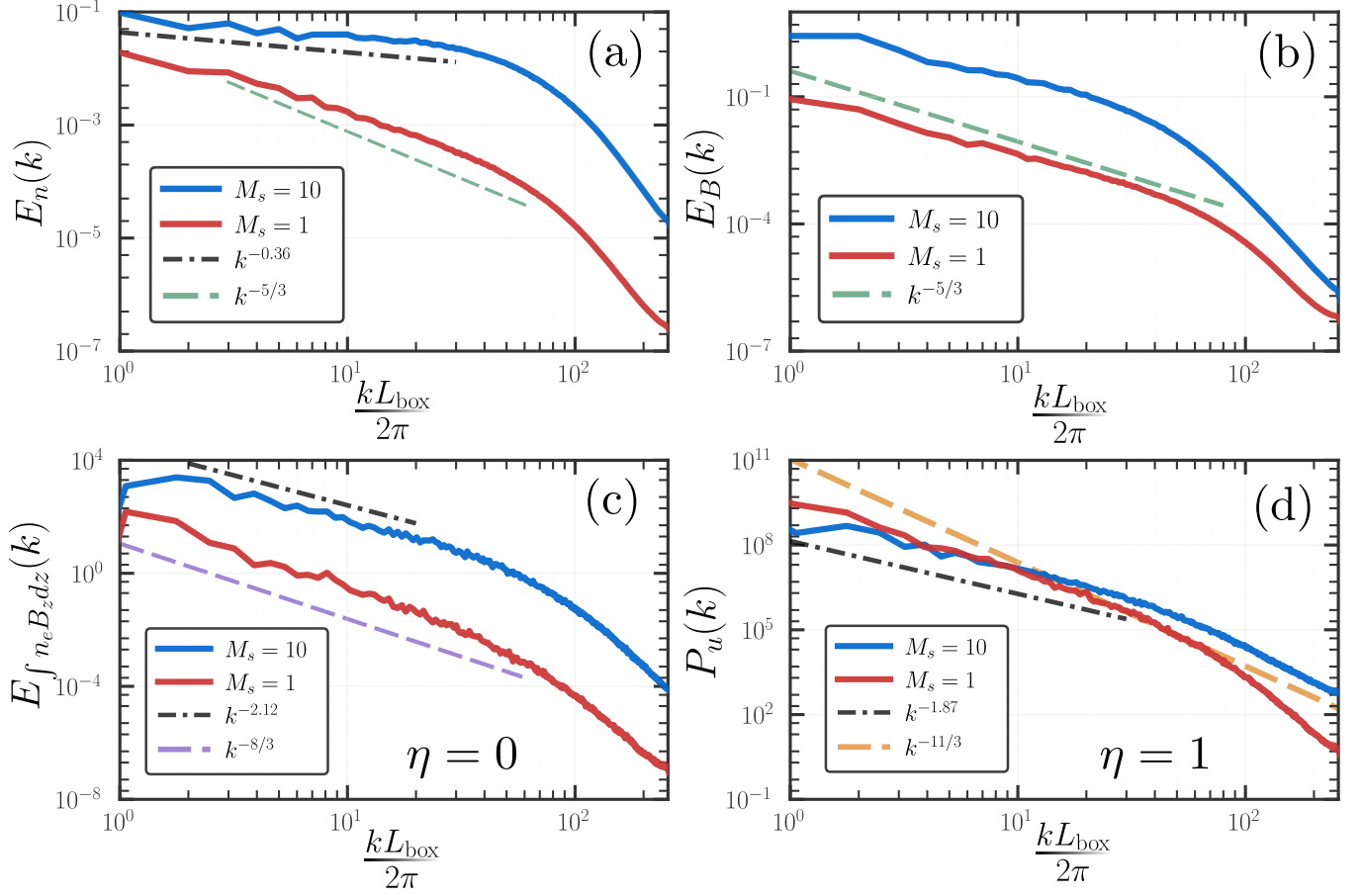


Figure 3. *Panel a:* Results of the MHD ATHENA-K simulations for sub-Alfvénic turbulence ($M_A = 0.8$) in the transonic ($M_s = 1.0$, red) and highly supersonic ($M_s = 10$, blue) regimes. The plotted $E_n(k)$ is the annularly integrated 2D spectrum of column-density fluctuations from the projected map, integrated over the emitting back three-quarter portion of the LOS; it is computed from the 2D Fourier power by summing over rings of constant projected wavenumber (so E_n is a fluctuation power and variance spectrum, not kinetic energy). *Panel b:* Column-density spectrum $E_n(k)$, integrated over the emitting (back three-quarter) portion of the LOS, shown together with the projected magnetic-field spectrum $E_B(k)$ over the same integration depth. The plotted $E_B(k)$ is the annularly integrated (ring-summed) 2D spectrum of the projected magnetic-field map, computed by summing the 2D Fourier power over rings of constant projected wavenumber. *Panel c:* shows the energy spectrum of direct integration $\int n_e B_z dz$. We see a clear $k^{-8/3}$ where k comes from the integration on the projection. *Panel d:* includes the directional spectrum generated by taking (25) for transonic and supersonic regimes, where the kolmogorov powerlaw $k^{-11/3}$ is followed and there are no slope break for $M_s = 1$; with $M_s = 10$, .

6.2. Wavelength derivative $dP/d\lambda^2$

The derivative of the polarization field with respect to the (square of) wavelength was another statistics, suggested by LP16. From

$$\frac{dP}{d\lambda^2} = 2i \Phi(\mathbf{X}) P(\mathbf{X}, \lambda^2), \quad (33)$$

we see that taking the derivative explicitly weights the signal by the foreground RM, potentially reflecting RM factor even at very short wavelength. LP16 showed that in the weak-decorrelation regime the structure function of $dP/d\lambda^2$ is sensitive to Faraday rotation without the λ^4 suppression that limits D_P . This makes $dP/d\lambda^2$ an excellent Faraday amplifier.

However, it comes at an observational cost: estimating $dP/d\lambda^2$ requires accurate multi-frequency measurements

and can amplify noise. Our angle-based statistic can be constructed from a single (Q, U) map and evaluated via a single FFT (Eq. 25).

For the separated-screen regime with weak-to-moderate Faraday rotation, the directional spectrum shows greater sensitivity to the Faraday screen slope at fixed wavelength, because it directly traces angle differences rather than amplitude-weighted correlations. The $dP/d\lambda^2$ measure has comparable or better sensitivity in the strong-rotation regime, but requires multi-frequency data.

The three measures are complementary: D_P constrains the emitting-region statistics at high frequency; $dP/d\lambda^2$ is a powerful Faraday amplifier when frequency precision is sufficient; and P_u provides an amplitude-independent, π -

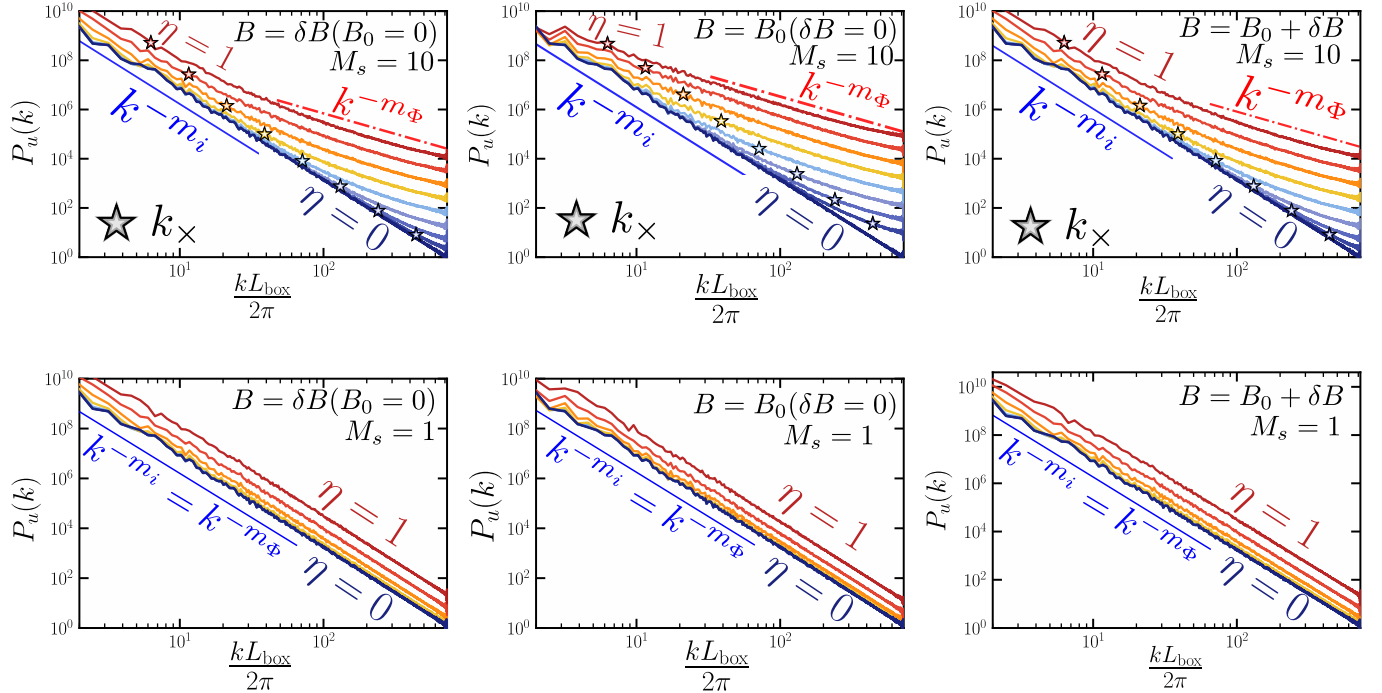


Figure 4. Directional spectrum $P_u(k; \lambda)$ from 1024^3 synthetic separated-screen experiments, illustrating the effect of mean-field and B_{\parallel} fluctuations. *Top row:* $M_s = 10$ ($\bar{n}/\sigma_n = 0.54$, $\bar{B}_{\perp}/\sigma_{B_{\perp}} = 6.33$). *Bottom row:* $M_s = 1$ ($\bar{n}/\sigma_n = 2.51$, $\bar{B}_{\perp}/\sigma_{B_{\perp}} = 3.55$). *Left:* zero-mean case ($B_0 = 0$). *Middle:* density-only screen ($B_{\parallel} = B_0 = \text{const}$). *Right:* full screen ($B_{\parallel} = B_0 + \delta B$). The mean field does not qualitatively alter the two-slope structure, while reduced B_{\parallel} fluctuations sharpen the spectral transition.

periodic, anisotropy-aware probe that is straightforward to implement from a single band.

7. DISCUSSION AND CONCLUSIONS

7.1. Summary of the directional spectrum

The principal advance of this work is the demonstration that the inertial-range statistics of a foreground Faraday screen can be recovered from a single radio-frequency polarization map. The directional spectrum, constructed from the Fourier transform of the amplitude-normalized Stokes field $u = (Q + iU)/\sqrt{Q^2 + U^2}$, inherits the π -periodicity of the polarization angle, avoids branch-cut ambiguities, and can be computed with a single fast Fourier transform. Both our ATHENAK MHD simulations and the controlled synthetic-screen experiments confirm that this estimator faithfully traces the underlying magnetic turbulence spectrum. At weak Faraday rotation the directional spectrum follows the intrinsic synchrotron slope; as the rms of RM η increases, a shallower Faraday-dominated regime emerges at high wavenumber, and the transition scale k_{\times} shifts to lower k in agreement with the analytical prediction of Eq. (23).

7.2. Comparison with earlier diagnostics

The results presented here complement and extend the theoretical framework of LP16. That study introduced position–frequency statistics of polarized synchrotron emission and showed that the wavelength derivative $dP/d\lambda^2$ acts

as a powerful Faraday amplifier: its structure function is sensitive to Faraday rotation even in the weak-decorrelation regime, without the λ^4 suppression that limits the standard polarization structure function D_P . However, estimating $dP/d\lambda^2$ requires accurate multi-frequency observations and can amplify noise.

By contrast, the directional spectrum operates entirely at a single frequency. Our comparison of both the structure functions and spectra of the newly introduced measures with the previous ones (Fig. 6 and 6) shows that, at moderate Faraday rotation, the directional spectrum exhibits greater sensitivity to the Faraday screen slope than the $dP/d\lambda^2$ measure, because it directly traces angle differences rather than amplitude-weighted correlations. In physical terms, amplitude normalization strips the intrinsic synchrotron brightness variations from the signal and exposes the Faraday-angle imprint. The $dP/d\lambda^2$ measure regains comparable or superior sensitivity only in the strong-rotation regime, where the Faraday factor dominates the full polarization signal, but at the cost of spectral differentiation.

The three diagnostics are therefore best viewed as complementary rather than competing. The polarization structure function D_P constrains the emitting-region statistics at high frequency where Faraday effects are negligible. The derivative $dP/d\lambda^2$ is a powerful Faraday amplifier when sufficient frequency precision is available. The directional spectrum provides an amplitude-independent, single-band probe that is

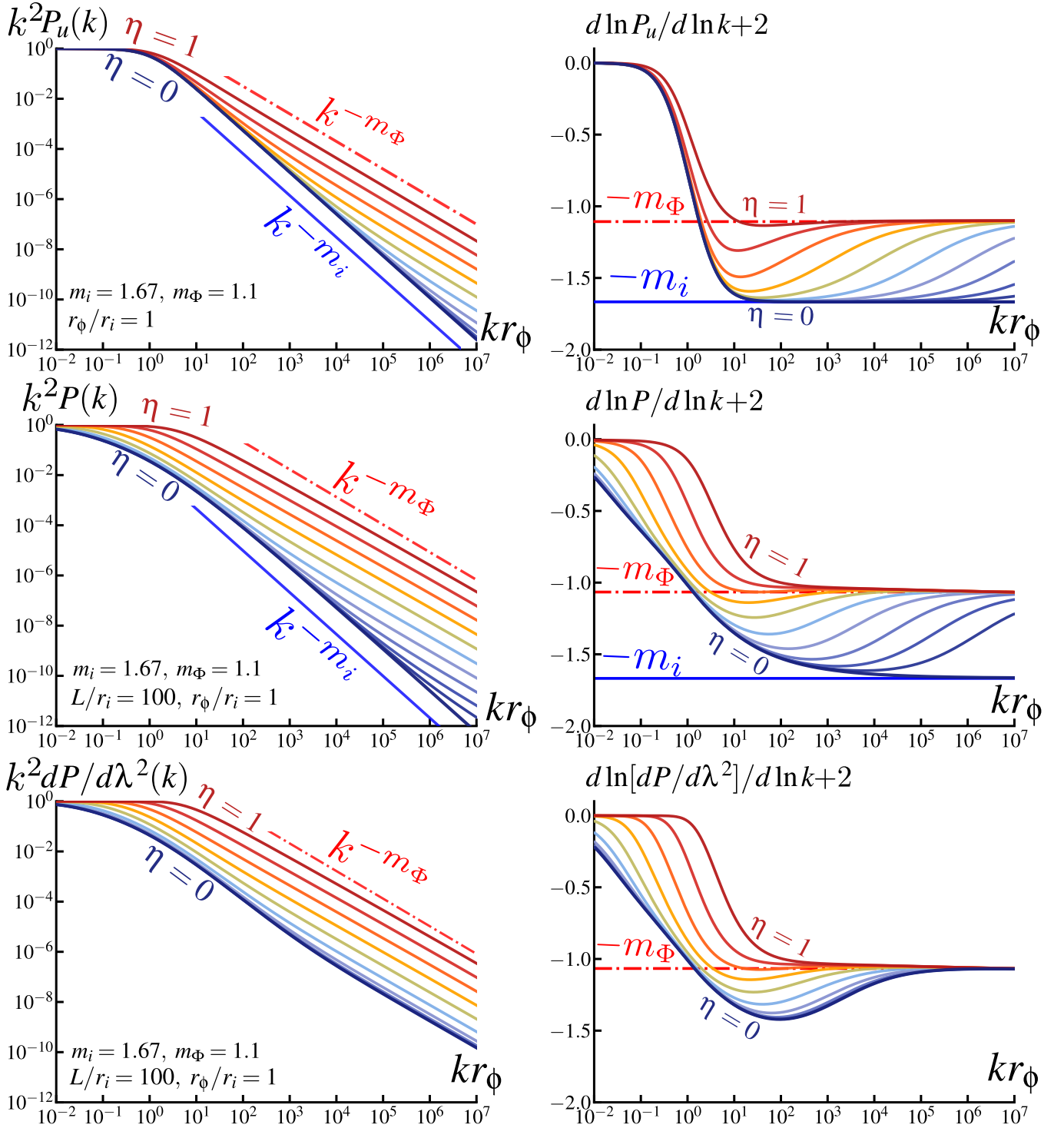


Figure 5. Comparison of spectrum for directional spectrum with measures introduced in LP16: the spectrum of polarization P and derivative polarization $dP/d\lambda^2$.

straightforward to implement and that responds to the Faraday screen across a broad range of rotation strengths.

Earlier angle-based studies, including classical Davis–Chandrasekhar–Fermi methods and modern dispersion function refinements (Davis 1951; Chandrasekhar & Fermi 1953;

Hildebrand et al. 2009; Houde et al. 2011), have used polarization-angle two-point statistics to infer the plane-of-sky magnetic field. The directional spectrum extends these ideas to the Faraday-screen setting by exploiting the explicit

$\lambda^4 D_\Phi(R)$ dependence, providing a pathway to inertial-range slope recovery rather than solely a field-strength estimate.

7.3. Observational criteria and practical considerations

A key practical outcome of this work is a simple, observable criterion that guides frequency requirements. The behavior of the bounded angle structure function $D_u(R; \lambda) = 2[1 - e^{-2\lambda^4 D_\Phi(R)}]$ is controlled by the product $\lambda^4 D_\Phi(R)$: when this quantity is small across the inertial range, D_u linearizes to $\lambda^4 D_\Phi$ and the turbulence slope is directly readable from a single map; when it approaches unity at small scales, the exponential saturates and the slope is compressed. In the transitional regime, two nearby frequency bands suffice to bracket the saturation and restore the correct spectral index. Only when the entire inertial range is saturated is full multi-frequency synthesis required.

An observer can therefore adopt the following strategy: compute the directional spectrum from an existing single-band (Q, U) map; check whether the measured slope steepens toward the saturation floor; and, if it does, add one adjacent band to interpolate through the transition. This approach significantly lowers the data requirements compared with full RM synthesis or derivative-based methods and is well suited to the separated-screen geometry common in Galactic and extragalactic radio polarimetry.

7.4. Limitations and future work

Several idealizations in the present analysis should be relaxed in future work. First, we have assumed a Gaussian distribution of RM increments; while this is well justified when the magnetic field dominates the RM fluctuations (Lazarian & Pogosyan 2016), highly supersonic turbulence can produce intermittent, non-Gaussian electron-density fields whose effect on the exponential damping factor warrants further study. Second, our separated-screen geometry neglects the internal depolarization that arises when emission and rotation are cospatial. Extending the directional-spectrum formalism to the mixed case treated by LP16 is a natural next step, particularly for low-frequency observations where internal Faraday rotation is strongest. Third, the 512^3 MHD grid affords only about one decade of inertial range; higher-resolution simulations would tighten the slope measurements and permit a quantitative assessment of the two-slope crossover in the self-consistent setting.

Despite these caveats, the present results establish the directional spectrum as a practical, single-frequency diagnostic of magnetized turbulence. Its minimal data requirements, robustness to amplitude calibration, and natural compatibility with interferometric baselines—where the Fourier-space estimator mirrors the visibility-plane measurement—make it well suited for application to current facilities and to forthcoming surveys with the Square Kilometre Array and its precursors.

7.5. Conclusions

The main conclusions of this work are as follows.

1. We introduced the directional spectrum, a Fourier-space estimator built from the amplitude-normalized Stokes field, and showed that it recovers the inertial-range scaling of a foreground Faraday screen from a single radio-frequency polarization map without RM synthesis or broad spectral coverage.
2. Using both self-consistent ATHENAK MHD simulations and controlled synthetic Faraday screens, we demonstrated that the directional spectrum transitions from the intrinsic synchrotron slope at weak Faraday rotation to a shallower Faraday-dominated regime at moderate-to-strong rotation.
3. Compared with the wavelength-derivative diagnostic of LP16, the directional spectrum exhibits greater sensitivity to the Faraday screen at moderate rotation strengths, because amplitude normalization strips intrinsic brightness variations and directly exposes the Faraday-angle imprint. The two measures are complementary: the derivative excels when multi-frequency data are available, while the directional spectrum operates at a single frequency.
4. We provided an observable criterion, rotation measure strength, based on the product of the rotation dispersion and wavelength, that indicates when a single band suffices for slope recovery, when two nearby bands are needed in the transitional regime, and when full multi-frequency synthesis is required.
5. Our results open a practical pathway to extract three-dimensional magnetic turbulence statistics from existing and forthcoming single-band radio polarimetry, lowering the data requirements relative to multi-frequency techniques and complementing them in a synergetic manner.

APPENDIX

A. STRUCTURE FUNCTION FOR POLARIZATION DIRECTIONS

Based on the obtained results for the analytical prediction of the structure function $D_u/2$ from (18), similar to the results of 6, we can analyze not only directional spectrum but its structure function as well. Figure 6 summarizes the real-space comparison of the three diagnostics discussed in the main text: the director-field structure function $D_u(R; \lambda)/2$, the LP16 polarization structure function $D_P(R)/D_P(\infty)$, and the derivative-based measure $D_{dP}(R)/D_{dP,\max}$. For each statistic, the left panel shows the structure function and the right panel shows the local logarithmic slope $d \ln(\cdot)/d \ln R$ for increasing Faraday-rotation strength η (blue to red). The reference lines with slopes m_i and m_Φ highlight the transition from the intrinsic-dominated regime to the Faraday-dominated regime as η increases. This figure provides the real-space counterpart to the spectral comparison in Fig. 6 and illustrates why the directional statistic responds strongly to the Faraday-screen scaling at moderate η .

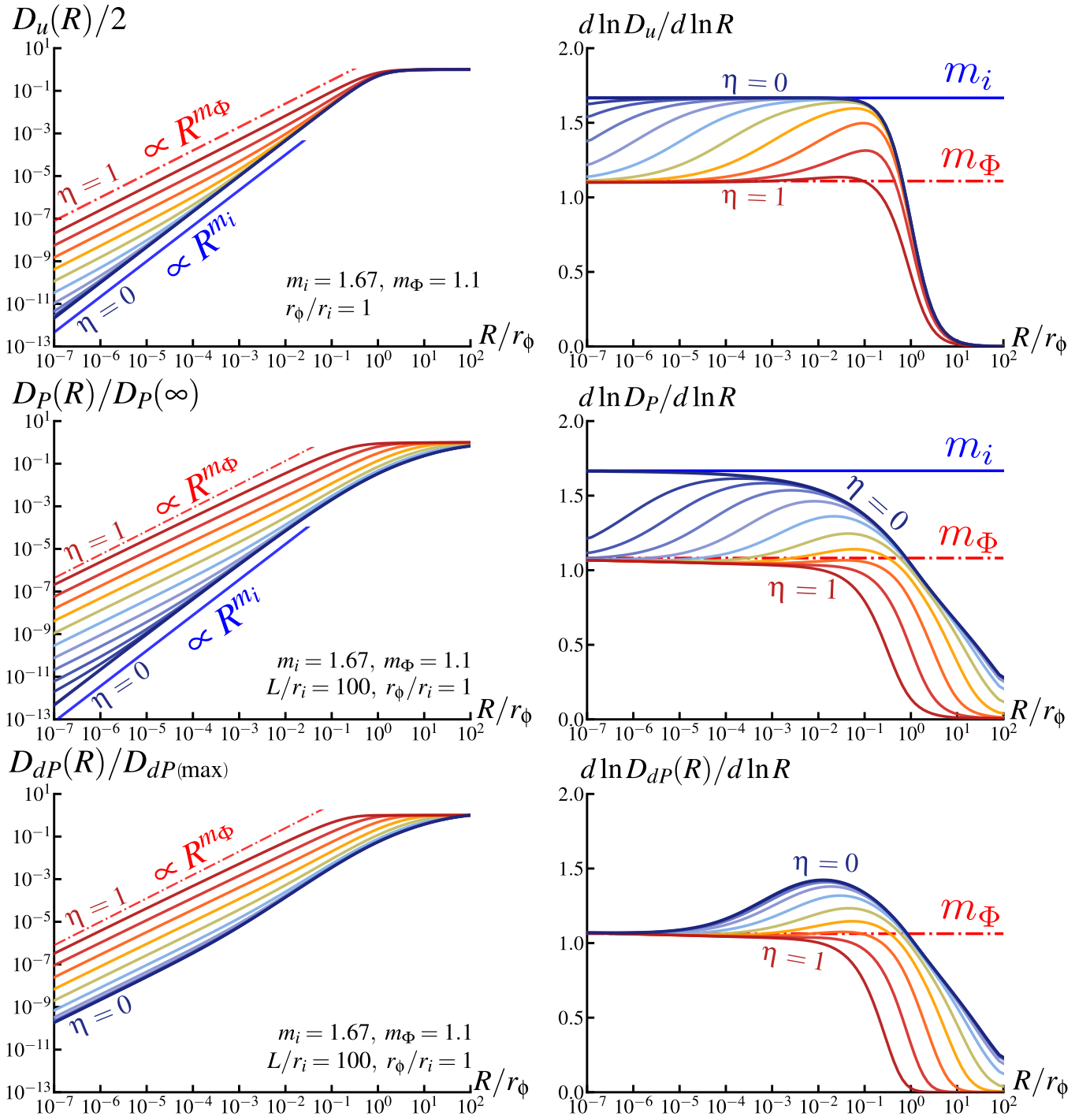


Figure 6. Comparison of structure-function of directional measure with measures introduced in **LP16** in the separated-screen model for increasing Faraday rotation strength η (colored curves; blue \rightarrow red for small \rightarrow large η , with $\eta = 0$ and 10 logarithmically spaced values from 3×10^{-3} to 1). The *left column* shows the structure functions, and the *right column* shows their local logarithmic slopes $d \ln(\cdot)/d \ln R$. *Top row*: the directional structure function $D_u(R; \lambda)/2$ from the weak-rotation ansatz (Eq. 18). *Middle row*: the normalized polarization structure function $D_P(R)/D_P(\infty)$ computed with the **LP16** kernel formalism. *Bottom row*: the **LP16** derivative-based measure, shown as the normalized structure function $D_{dP}(R)/D_{dP,\max}$ (constructed from $dP/d\lambda^2$). In all rows, the blue solid and red dot-dashed guide lines mark the expected inertial-range scalings $\propto R^{m_i}$ and $\propto R^{m_\Phi}$, respectively (here $m_i = 5/3$ and $m_\Phi = 1.1$, following synthetic cube results; R is plotted in units of r_ϕ , with $r_\phi = r_i$ in this example). As η increases, the Faraday contribution expands and the slope transitions from the intrinsic asymptotics (m_i) to the Faraday-screen asymptotics (m_Φ), making the analysis of structure function D_u complementary to the studying of the directional spectrum P_u .

REFERENCES

- Akahori, T., Nakanishi, H., Sofue, Y., et al. 2018, *PASJ*, 70, R2, doi: [10.1093/pasj/psx123](https://doi.org/10.1093/pasj/psx123)
- Armstrong, J. W., Rickett, B. J., & Spangler, S. R. 1995, *ApJ*, 443, 209, doi: [10.1086/175515](https://doi.org/10.1086/175515)
- Balbus, S. A., & Hawley, J. F. 1991, *ApJ*, 376, 214, doi: [10.1086/170270](https://doi.org/10.1086/170270)
- Beck, R. 2015, *A&A Rv*, 24, 4, doi: [10.1007/s00159-015-0084-4](https://doi.org/10.1007/s00159-015-0084-4)
- Brandenburg, A., & Lazarian, A. 2013, *SSRv*, 178, 163, doi: [10.1007/s11214-013-0009-3](https://doi.org/10.1007/s11214-013-0009-3)
- Brentjens, M. A., & de Bruyn, A. G. 2005, *A&A*, 441, 1217, doi: [10.1051/0004-6361:20052990](https://doi.org/10.1051/0004-6361:20052990)
- Burn, B. J. 1966, *MNRAS*, 133, 67, doi: [10.1093/mnras/133.1.67](https://doi.org/10.1093/mnras/133.1.67)
- Chandrasekhar, S., & Fermi, E. 1953, *ApJ*, 118, 113, doi: [10.1086/145731](https://doi.org/10.1086/145731)
- Davis, L. 1951, *Physical Review*, 81, 890, doi: [10.1103/PhysRev.81.890.2](https://doi.org/10.1103/PhysRev.81.890.2)
- Elmegreen, B. G., & Scalo, J. 2004, *ARA&A*, 42, 211, doi: [10.1146/annurev.astro.41.011802.094859](https://doi.org/10.1146/annurev.astro.41.011802.094859)
- Falceta-Gonçalves, D., Lazarian, A., & Kowal, G. 2008, *ApJ*, 679, 537, doi: [10.1086/587479](https://doi.org/10.1086/587479)
- Federrath, C. 2018, *Physics Today*, 71, 38, doi: [10.1063/PT.3.3947](https://doi.org/10.1063/PT.3.3947)
- Goldreich, P., & Sridhar, S. 1995, *ApJ*, 438, 763, doi: [10.1086/175121](https://doi.org/10.1086/175121)
- Haverkorn, M. 2015, in *Astrophysics and Space Science Library*, Vol. 407, *Magnetic Fields in Diffuse Media*, ed. A. Lazarian, E. M. de Gouveia Dal Pino, & C. Melioli, 483, doi: [10.1007/978-3-662-44625-6_17](https://doi.org/10.1007/978-3-662-44625-6_17)
- Herron, C. A., Burkhart, B., Lazarian, A., Gaensler, B. M., & McClure-Griffiths, N. M. 2016, *ApJ*, 822, 13, doi: [10.3847/0004-637X/822/1/13](https://doi.org/10.3847/0004-637X/822/1/13)
- Hildebrand, R. H., Kirby, L., Dotson, J. L., Houde, M., & Vaillancourt, J. E. 2009, *ApJ*, 696, 567, doi: [10.1088/0004-637X/696/1/567](https://doi.org/10.1088/0004-637X/696/1/567)
- Houde, M., Rao, R., Vaillancourt, J. E., & Hildebrand, R. H. 2011, *ApJ*, 733, 109, doi: [10.1088/0004-637X/733/2/109](https://doi.org/10.1088/0004-637X/733/2/109)
- Houde, M., Vaillancourt, J. E., Hildebrand, R. H., Chitsazzadeh, S., & Kirby, L. 2009, *ApJ*, 706, 1504, doi: [10.1088/0004-637X/706/2/1504](https://doi.org/10.1088/0004-637X/706/2/1504)
- Hu, Y., Xu, S., Arzamasskiy, L., Stone, J. M., & Lazarian, A. 2024, *MNRAS*, 527, 3945, doi: [10.1093/mnras/stad3493](https://doi.org/10.1093/mnras/stad3493)
- Jansson, R., & Farrar, G. R. 2012, *ApJ*, 757, 14, doi: [10.1088/0004-637X/757/1/14](https://doi.org/10.1088/0004-637X/757/1/14)
- Lazarian, A., & Pogosyan, D. 2012, *ApJ*, 747, 5, doi: [10.1088/0004-637X/747/1/5](https://doi.org/10.1088/0004-637X/747/1/5)
- . 2016, *ApJ*, 818, 178, doi: [10.3847/0004-637X/818/2/178](https://doi.org/10.3847/0004-637X/818/2/178)
- Lazarian, A., Yuen, K. H., Lee, H., & Cho, J. 2017, *ApJ*, 842, 30, doi: [10.3847/1538-4357/aa74c6](https://doi.org/10.3847/1538-4357/aa74c6)
- Lazarian, A., Yuen, K. H., & Pogosyan, D. 2022, *ApJ*, 935, 77, doi: [10.3847/1538-4357/ac6877](https://doi.org/10.3847/1538-4357/ac6877)
- Oppermann, N., Junklewitz, H., Robbers, G., et al. 2012, *A&A*, 542, A93, doi: [10.1051/0004-6361/201118526](https://doi.org/10.1051/0004-6361/201118526)
- Sokoloff, D. D., Bykov, A. A., Shukurov, A., et al. 1999, *MNRAS*, 303, 207, doi: [10.1046/j.1365-8711.1999.02161.x](https://doi.org/10.1046/j.1365-8711.1999.02161.x)
- Stone, J. M., Mullen, P. D., Fielding, D., et al. 2024, *arXiv e-prints*, arXiv:2409.16053, doi: [10.48550/arXiv.2409.16053](https://doi.org/10.48550/arXiv.2409.16053)
- Taylor, A. R., Stil, J. M., & Sunstrum, C. 2009, *ApJ*, 702, 1230, doi: [10.1088/0004-637X/702/2/1230](https://doi.org/10.1088/0004-637X/702/2/1230)
- Xiao, Y.-W., Zhang, J.-F., Lazarian, A., & Pogosyan, D. 2025, *ApJ*, 990, 169, doi: [10.3847/1538-4357/adf850](https://doi.org/10.3847/1538-4357/adf850)
- Zhang, J.-F., Lazarian, A., Lee, H., & Cho, J. 2016, *ApJ*, 825, 154, doi: [10.3847/0004-637X/825/2/154](https://doi.org/10.3847/0004-637X/825/2/154)
- Zhang, X.-W., Zhang, J.-F., Wang, R.-Y., & Xiang, F.-Y. 2023, *MNRAS*, 523, 5748, doi: [10.1093/mnras/stad1785](https://doi.org/10.1093/mnras/stad1785)